Catalytic Fe-*x*N Sites in Carbon Nanotubes

Alexey Titov,[†] Peter Zapol,*[,‡] Petr Král,*[,†] Di-Jia Liu,[§] Hakim Iddir,[‡] Kopinjol Baishya,[¶] and Larry A. Curtiss[‡,⊥]

Department of Chemistry, University of Illinois at Chicago, Chicago, Illinois 60607, Materials Science Division, Argonne National Laboratory, Argonne, Illinois 60439, Chemical Sciences and Engineering Division, Argonne National Laboratory, Argonne, Illinois 60439, and Department of Physics, University of Illinois at Chicago, Chicago, Illinois 60607, and Center for Nanoscale Materials, Argonne National Laboratory, Argonne, Illinois 60439

Received: December 8, 2008; Revised Manuscript Received: September 3, 2009

To reduce fuel cell cost, durable and inexpensive electrode catalysts need to be developed to replace precious metal materials, particularly for the electrocatalytic oxygen reduction at cathodes. In this study, we explored the structure and the energetics of Fe-*x*N ($x = 2,4$) incorporated into carbon nanotubes and graphene using density functional theory to show that these structures are more stable than iron atoms on nanotubes and that pyridinic structures of Fe-4N are more favorable than pyrrolic structures. EXAFS spectra simulated from the optimized structures show good agreement with results of measurements obtained on arrays of aligned nanotubes doped with iron and nitrogen, which have demonstrated activity toward oxygen-reduction reactions.

Introduction

Developing a proton-exchange membrane fuel cell (PEMFC) as a highly efficient, H_2-powered electricity generation device has attracted extensive efforts.[1,2] For a PEMFC, the energy conversion efficiency is predominantly limited by the electrocatalytic oxygen-reduction reaction (ORR) rate[3] on the cathode side due to the sluggish kinetics. At present, the most effective ORR catalysts are made of precious group metals (PGMs), such as platinum or platinum alloys.[4−7] High price and limited reserves of PGMs add significant cost to the fuel cell system and create a major barrier for its commercialization. There is a clear demand and urgency to develop low-cost, non-PGM-based electrode catalysts.[8] Various non-PGM materials have been evaluated as the alternative cathode catalysts for fuel cells, including N-coordinated transition-metal (TM) macromolecules,[9−11] nitrogen- and TM-doped carbon and carbon nanotubes,[12−14,14−16,16−21] chalcogenides,[22−25] oxynitrides and carbonitrides,[26−29] TM-doped conductive polymers,[30] etc. A summary of the research can be found in a recent review article by Borup et al.[31]

Among non-PGM catalysts, we are particularly interested in TM/N macromolecules and TM/N carbonaceous materials. For example, TM/N macromolecules mimic natural systems, such as metallo−porphyrin complexes (hemes), which activate many biochemical reactions.[9,10] Early experiments observed the catalytic activity of Co-phthalocyanines in ORR reactions.[11] Such systems led to the extension of the investigations on TM(Fe,Co)/N-doped carbon catalysts.[12−15] In particular, Dodelet and co-workers[14,16−18,32] have studied extensively Fe and Co on nitrogen-modified carbon supports obtained by high-temperature pyrolysis using a variety of precursors. They found, for example, that the increase of N content in iron-doped carbon promotes the formation of $Fe_xC_{1-x-y}N_y$, which leads to an increase in catalytic activity. The activity was influenced by both the structure of the catalytic site and the modification of the support. In addition to TM/N-doped carbons prepared through pyrolysis, other nitrogenated bulk[16,18] and nanostructured[19,20,33] carbonaceous materials were also found to manifest some ORR activity. In particular, a recent study demonstrated ORR activity of aligned carbon nanotubes incorporated with atomically dispersed iron and nitrogen prepared through a chemical vapor deposition process.[21] Aligned carbon nanotubes could offer some unique advantages in the electrochemical and fuel cell applications. In addition to high surface area, aligned CNTs as the electrode and the catalyst can establish excellent thermal and electro-conductivities through direct contact between the catalytic surface and the current collector.[34] The graphitic nature of CNTs also improves the oxidative corrosion resistance that is crucial for the catalytic application at cathode. In Fe- and N-doped aligned CNTs, Fe-4N catalytic sites with square-planar configuration were found to be embedded onto the nanotube walls and *distributed* uniformly throughout the whole tube.[21] In fact, experimental studies on these systems report the detection of catalytic activity and preliminary results on in situ XAS studies.[35] This motivates us to study the structure and the stability of possible catalytic sites.

In this study, we combine theoretical and experimental approaches to investigate the stability of Fe-*x*N catalytic sites embedded in CNTs prepared by the chemical vapor deposition. Several theoretical studies have addressed the structure and activity of graphite with nitrogen and iron incorporation.[36,37] Recently, we investigated metal−nitrogen incorporation in carboneous nanostructures[38−40] and studied other chemically reactive sites, such as "bumpy" structures on CNTs.[41] Here, we investigate the properties of iron and nitrogen sites in CNT and graphene systems and compare simulated EXAFS spectra to the experimental data for such sites in aligned CNT arrays. The active sites in multiwalled nanotubes are also likely to be associated with the outer surface of the tube since interlayer

* To whom correspondence should be addressed. E-mail: zapol@anl.gov (P.Z.), pkral@uic.edu (P.K.).
[†] Department of Chemistry, University of Illinois at Chicago.
[‡] Materials Science Division, Argonne National Laboratory.
[§] Chemical Sciences and Engineering Division, Argonne National Laboratory.
[¶] Department of Physics, University of Illinois at Chicago.
[⊥] Center for Nanoscale Materials, Argonne National Laboratory.

10.1021/jp810792d
Published on Web 12/03/2009

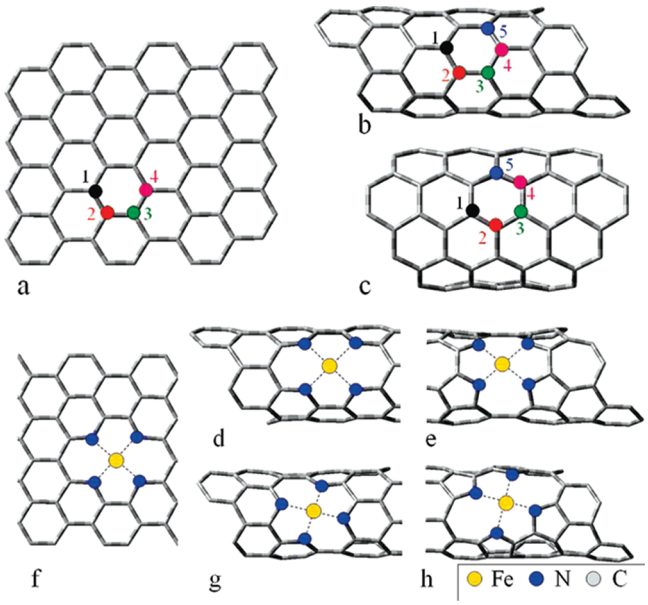

Figure 1. (top) Nitrogen atoms are substituted into (a) planar graphene, (b) (7,0) CNT, and (c) (5,5) CNT. (bottom) The Fe-N $_4$ sites are shown for (f) the graphene sheet and (d, e, g, h) (7,0) CNT clusters. The pyridinic and pyrrolic Fe configurations are shown in (d, g) and (e, h), respectively. The configurations are in axial (d, e) or in helical orientation (g, h). The terminating hydrogens are not shown.

confinement would impede transport of species. These results can be used as a guideline for a rational design of new catalysts for the ORR.

Theoretical Modeling

Models and Methods. First-principles calculations of model systems representing Fe-*x*N catalytic sites embedded in CNTs are performed at the density functional theory (DFT) level with the B3LYP hybrid exchange-correlation functional, as implemented in Gaussian 03.[42] We use the 6-31G* Gaussian basis sets for C, N, Fe, and H atoms. A cluster approach is chosen to construct models of the active site incorporated into a graphene sheet or CNTs. To analyze the curvature effect of the CNTs in the calculations, we use bent clusters cut from the nanotubes with edge carbon atoms terminated by hydrogen atoms. To maintain the desired surface curvature, hydrogens at the edges of the clusters are kept fixed during the optimization of the molecular geometry. The planar model is a limiting approximation to the low-curvature multiwalled CNT outer surface in the recent experiments.[21] The cluster models of the planar graphene, shown in Figure 1a, and the zigzag (8,0) CNT (not shown) have 24 hexagonal carbon rings. The clusters representing the (7,0) CNT and the (5,5) CNT have 23 hexagonal carbon rings, as shown in Figure 1b,c, respectively.

We study structures with two and four N substitutions and optimize them without and with a single Fe atom attached to them. Three-nitrogen structures are not studied since there is no experimental evidence for their stability. The cluster models of CNTs and graphene with the enumeration of their atoms that is used in nitrogen substitution notations are shown in Figure 1a−c. The position of the Fe atom is optimized around the two N atoms (see the Supporting Information, Figures S5−S27).

Each pair of the carbons labeled 1-2, 1-3, and 1-4 is substituted by two N atoms to obtain the corresponding 2N structure. The axial symmetry of the nanotubes introduces three additional nonequivalent configurations. In total, the nanotubes have six configurations along the symmetry axis and at various

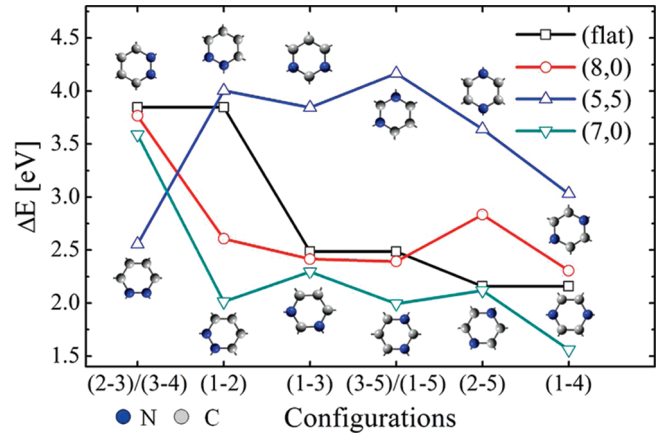

Figure 2. Substitution energies ΔE_{2N} (eq 1) are shown for the planar and curved clusters. On the horizontal axis, the configurations of the two N substitutions are shown for the zigzag/armchair nanotube clusters, as schematically represented by the six-membered carbon rings on the top (bottom) of the graph for the armchair (zigzag) nanotube clusters. The symmetry axis of the CNTs is oriented horizontally. In the flat graphene, the N configurations are double degenerate.

angles to it, respectively, as shown in Figure 1b,c. We call a configuration with two nitrogens *axial* (AX), if the vector connecting nitrogens is parallel to the nanotube axis, and *helical* (HE) in all the other cases. Thus, zigzag CNT clusters have axial configurations (2-3) and (1-4) for the nearest-neighbor and the third-nearest-neighbor nitrogens, respectively. In addition, the zigzag (7,0) CNT in Figure 1b has four HE configurations: the nearest-neighbor (1-2), the next-nearest-neighbor (2-4) and (3-5), and the third-nearest-neighbor configurations (2-5). The armchair (5,5) CNT in Figure 1c has one AX and five HE configurations: (1,3), (1,2), (1,4), (1,5), (2,5), and (3,4), respectively.

The Fe-4N sites have porphyrin-like configurations, where the Fe atom is coordinated by four N atoms, incorporated in pyridinic (PD) six-membered or pyrrolic (PL) five-membered rings, shown in Figure 1d,g and e,h, respectively. These structures are obtained by the substitution of six carbon atoms by four nitrogens. Because CNTs have an axial symmetry, there are twice as many configurations as in the planar graphene (see the Supporting Information, Figures S27−S40). In the CNT cluster models, we denote the structures according to the orientation of the rectangular N coordination shell with respect to the nanotube axis. We call it axial (AX) if one of the N−N axis is parallel to the CNT axis (Figure 1d,e) and as helical (HE) otherwise (Figure 1g,h).

Energetics of the Metal-Free Structures. We compare the stability of different configurations in the N-substituted carbon clusters and calculate the N-substitution energies using

$$\Delta E_{x\mathrm{N}} = E_{\mathrm{site}+x\mathrm{N}} + yE_{\mathrm{C}} - \left(E_{\mathrm{site}} + \frac{x}{2}E_{\mathrm{N}_2}\right) \qquad (1)$$

Here, E_{C} is the total energy of the nanotube per carbon atom and E_{site} and $E_{\mathrm{site}+x\mathrm{N}}$ are the energies of the cluster before and after N substitution, respectively.

The E_{N_2} term is the energy of an isolated N_2 molecule and x stands for the number of N atoms substituting y carbon atoms. The values of $x(y)$ are equal to 2(2) and to 4(6) in the case of two nitrogens and pyridinic (or pyrrolic) coordination, respectively.

Figure 2 summarizes the N-substitution energies in the carbon clusters with different configurations. We find that ΔE_{2N} is

TABLE 1: Substitution Energies ΔE_{4N} for the CNT Cluster Models[a]

configuration	(flat)	(8,0)	(5,5)	(7,0)
	4N substitution energies [eV]			
AXPD	5.47	3.90	5.59	3.96
HEPD	5.47	4.57	4.73	5.40
AXPL	10.79	7.85	8.67	7.34
HEPL	10.79	8.11	8.90	8.45
	Fe binding energy/Fe-4N substitution energies [eV]			
AXPD	−7.39/−1.92	−5.77/−1.87	−6.08/−0.49	−5.44/−1.48
HEPD	−7.39/−1.92	−5.98/−1.41	−6.60/−1.87	−6.45/−1.05
AXPL	−8.57/2.22	−8.33/−0.48	−7.83/0.84	−8.34/−1.00
HEPL	−8.57/2.22	−6.69/1.42	−6.27/2.63	−6.57/1.88

[a] Their curvature increases from the left to the right. Iron binding energies ΔE_{Fe} are calculated for the different 4N sites. Slash-separated values are the $\Delta E_{Fe\text{-}4N}$ substitution energies of Fe-4N sites in the carbon clusters. PD and PL refer to pyridinic and pyrrolic structures, respectively.

positive in all the cases, and thus, the substitution reaction is *endothermic*. For zigzag nanotubes, CNTs with a smaller radius tend to have lower substitution energies since the binding energy of substituted C atoms is lower for higher CNT curvature. The higher pyramidality of smaller radius nanotubes is also more favorable for N incorporation. Comparing our N_2 substitution energies with previous GGA calculations,[43] we find a similar trend that, although the nearest-neighbor nitrogens are energetically preferred for armchair (5,5) nanotube, the increase of distance between nitrogens lowers the substitution energy for zigzag nanotubes. We also find that planar graphene exhibits substitution behavior similar to that of zigzag nanotubes. Although the ΔE_{2N} energies are positive, the obtained structures are local minima and their energy is further lowered by the addition of metal atoms,[39] which supports the experimental observation on Fe incorporation in N-doped nanotubes.[34]

The results obtained from eq 1 for four-N substitutions are summarized in Table 1. From the energies, we can see that a release of spatial strain in zigzag CNTs might be facilitated in the axial rather than helical configurations, which typically have lower ΔE_{4N}. In armchair CNTs, the situation is exactly opposite. The origin of this behavior is in the inequivalent sides of the rectangle formed by four nitrogens because of the difference in their second neighbor shells, which is quite distinct from a square structure in porphyrins and phthalocyanines. In the (5,5) CNT cluster, the N rectangle has its longest side perpendicular to the tube axis. On the contrary, the orientation of the N rectangle in the (7,0) and (8,0) clusters is opposite, and substitution in this orientation is energetically less demanding. This results in a noticeably larger ΔE_{4N}, as seen in the first row of Table 1.

We also compare two different types of N substitutions. The pyrrolic configurations show the same trend in substitution energies as that of pyridinic configurations, but in the higher-energy range. The reason why the pyridinic coordination is preferred over the pyrrolic one is likely associated with the strain on the surrounding structure exerted by the five- and seven-membered carbon rings around each nitrogen in pyrrolic configuration, as seen in all columns of Table 1.

Energetics of the Fe-*x*N Structures. Iron atom incorporation is considered here for all calculated *x*N sites. In the case of two nitrogens, Fe is bound in the vicinity of two N atoms (Figure 1a−c). In porphyrin-like structures, an Fe atom is integrated into the plane of the site and coordinated by each of the four N atoms, as shown in Figure 1d−h. The results are reported for quintet and triplet spin states of the CNT cluster models with

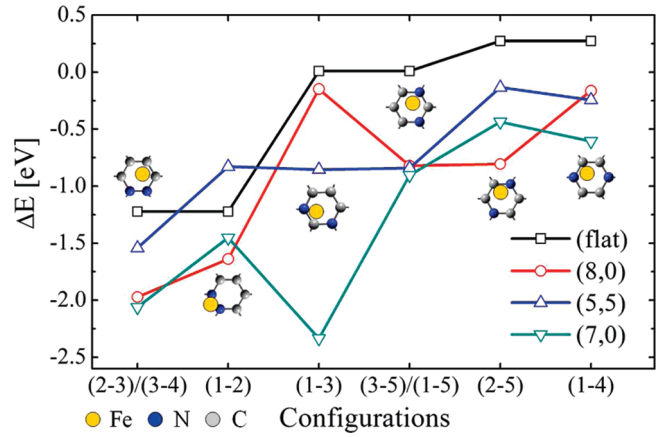

Figure 3. Fe adsorption energies $\Delta E_{Fe\text{-}2N}$ are shown for the planar and curved clusters. The resulting structures are shown schematically on the graph by the six-membered carbon rings where the CNT axis is oriented horizontally.

Fe-2N and Fe-4N, respectively. Our calculations with different multiplicities identify them as ground states.

The stability of the Fe-*x*N sites is evaluated through the adsorption energy of the Fe atom with the N-substituted support. We calculate the adsorption energy of Fe using the expression

$$\Delta E_{Fe} = E_{site+Fe} - (E_{site} + E_{Fe}) \quad (2)$$

where E_{Fe} is the energy of an isolated Fe atom and $E_{site+Fe}$ and E_{site} are the energies of clusters with and without Fe, respectively.

In Figure 3, we compare the adsorption energies ΔE_{Fe} of Fe binding to a flat graphene and curved surfaces of CNTs with two-nitrogen substitution. The flat cluster has the lowest binding energies. The energies increase with the curvature of the zigzag CNTs in the (2-3), (1-3), (3-5), and (1-4) configurations. Configurations of the armchair clusters have smaller binding energies ranging from −1.54 to −0.13 eV, possibly because of the lower stability of their respective 2N configurations, as shown in Figure 2. Overall, the sites with neighboring or next neighboring nitrogens are more stable in the presence of an Fe atom. The moderately favorable (1-3) configuration of nitrogens is greatly stabilized by the adsorption of Fe in the (7,0) nanotube cluster (compare Figures 2 and 3) and has the adsorption energy ΔE_{Fe} of −2.34 eV. In this configuration, the Fe atom is embedded into the surface of the cluster, in contrast to the other Fe-2N configurations, where an Fe atom primarily resides on the top of N atoms. The distance from the Fe atom to the surface of the (7,0) cluster is 1.12 Å and about 1.54−1.95 Å in (1-3) and the other configurations, respectively. High curvature of the (7,0) nanotube cluster and the position of the nitrogens allow the Fe atom to break two C−N bonds and to form four new bonds with Fe (as shown in the Supporting Information, Figure S22). However, such stabilization is highly sensitive to the curvature and relative positions of the nitrogens, so it is manifested only for the CNT with the smallest studied radius and results in binding energies of −0.13 and −0.85 eV for (8,0) and (5,5) CNT clusters, respectively. In comparison, the B3LYP binding energy for Fe interacting with an (8,0) nanotube is calculated to be −0.86 eV, whereas the Fe interaction with graphene was found to be slightly repulsive. Thus, the results in Figure 3 show that, in most cases, the addition of two nitrogens makes the Fe interaction more favorable.

In Table 1, we show the Fe binding energies for the pyridinic and pyrrolic Fe-4N catalytic sites. The curvature dependence

TABLE 2: Bond Lengths of the Fe Atom in the Planar and Bent Fe-*x*N Structures[a]

configuration	b_{flat}	$b_{(8,0)}$	$b_{(5,5)}$	$b_{(7,0)}$
		Fe-2N structures [Å]		
(1-2)	N(2.07) N(1.91) C(2.17) C(2.16)	N(2.01) N(1.92)	N(1.74) N(1.74)	N(2.05) N(1.92)
(1-3)	C(2.16) N(2.28) C(2.19)	N(1.86) C(1.83)	N(2.05) C(1.97)	C(1.87) N(1.91) C(1.97) N(1.96)
(2-3)/(3-4)		N(1.72) N(1.72)	N(1.92) N(1.91)	N(1.72) N(1.72)
(1-4)	C(2.20)	C(2.0) C(2.07) N(2.38)	C(2.14) N(2.19)	C(2.09) C(2.11)
(2-5)		C(2.12) N(2.14) C(2.07) C(2.08)	C(2.10) C(2.10) C(2.10) C(2.10)	N(2.09) C(2.03) C(2.16) C(2.15)
(3-5)/(1-5)		C(2.12) N(2.14) C(2.07) C(2.12)	C(2.12) C(2.13)	C(2.07) N(2.11) C(2.15)
		Fe-4N structures [Å]		
AX PD	1.87 (1.88)	1.97 (1.98)	1.87 (1.87)	2.00 (2.00)
HE PD	1.87 (1.88)	1.91 (1.92)	1.93 (1.96)	1.86 (1.91)
AX PL	1.90 (1.92)	1.87 (1.87)	1.94 (1.94)	1.87 (1.90)
HE PL	1.90 (1.92)	1.87 (2.03)	1.81 (2.02)	1.87 (2.07)
FePc	N(1.94) C(2.97)			

[a] Index stands for flat and bent (8,0), (5,5), and (7,0) clusters. The curvature of CNT clusters increases from left to right. (down) Fe−N bond lengths for the different Fe-4N sites. In the last row, we give the calculated distances between Fe and neighboring atoms in Fe-phthalocyanine.

of the axial PD sites in zigzag nanotubes (Figure 1d) is manifested through a slight decrease of the binding energy from flat to (7,0) clusters. On the contrary, HE PD sites (Figure 1g) do not show such a decrease in stability with the increasing curvature. This difference between the HE and AX configurations is associated with the orientation of five-membered C_2N_2Fe rings relative to the nanotube axis; the Fe−N bonds in helical configurations are also shorter (see Table 2). These results show that Fe adsorption is strongly dependent on the CNT curvature for small radii. The relative stability of the formed sites is also seen from the combined energies of the N incorporation and Fe adsorption, calculated from the sum $\Delta E_{Fe\text{-}4N} = \Delta E_{4N} + \Delta E_{Fe}$. Overall, the PD sites have greater stability than the PL sites, as shown in Table 1. This larger stability might be supported by the observation of pyridinic nitrogens in nitrogenated carbon supports.[16,33] Pyridinic compounds represent a very stable fraction and were associated with the most active catalytic sites.[16] By comparing NBO charges (see the Supporting Information, Table ST2) to the Fe-phthalocyanine, the oxidation state of iron in pyridinic configurations is close to that in Fe-phthalocyanine, which is +2. Fe(II) was shown to be electrochemically active, for example, by Yeager and co-workers.[44]

Additional calculations to analyze the charge distribution in the pyridinic and pyrrolic models were performed using the CNT (8,0) model for pyrrolic, pyrrolic without hydrogens, and Fe-pyrrolic structures as well as 2H-pyridinic, pyridinic, and Fe-pyridinic structures. The NBO charge distributions on hydrogens, nitrogens, and their neighbors are the same in the 2H-pyridinic and pyrrolic structures. When hydrogens are removed, the negative charge on nitrogen atoms is compensated by positive charges mainly on the nearest-neighbor carbon atoms in the two structures. The insertion of an iron atom results in electron transfer from this atom to the nitrogens in both pyrrolic and pyridinic structures. Detailed information on NBO charges is included in part 3 of the Supporting Information.

We obtain densities of states (see the Supporting Information, Figure S3) by the Gaussian broadening of the calculated cluster spectra for the flat PD Fe-4N configuration. The results indicate that Fe d states are strongly hybridized with the π states of carbon atoms. The validity of the approach is verified by comparing the total density of states for this structure to calculations on the same system using the periodic VASP code.[45,46] In the periodic case, the Fe-4N is substituted into a supercell of two-dimensional periodic graphene sheet, and the structure is optimized. The total density of states calculated in the cluster model agrees well with the periodic calculations. Therefore, the electronic properties from cluster calculations can be used to study the catalytic activity (see the Supporting Information, Figure S4).

Catalytic activity of transition-metal macrocyclic complexes toward oxygen reduction is often correlated with a first ionization potential of the complexes since the electron is extracted from the d states of the metal atom. Vertical ionization potentials (see the Supporting Information, Figure S1) are found to be in the range of 4.5−5.75 eV, depending on CNT curvature, which is well below reported values for Fe-porphyrins of 6.36 eV.[47] It can be explained by noticing that nanotubes by themselves have ionization potentials of about 4.86−5.08 eV (experiment 4.6−4.8 eV[48]), which is also consistent with our DOS indicating strong hybridization of iron d states and carbon p states. The lower ionization potential is often related to a lower redox potential and a higher oxidation activity.[49] Therefore, we expect Fe-4N complexes in CNTs to be more active in ORR as compared with other iron macrocycles.

Our calculations of oxygen adsorption on the iron atom in Fe-4N structures give O_2 binding energies of 0.78 eV for the (7,0) CNT cluster, which is similar to porphyrins.[49]

Bond Lengths of the Fe-*x*N Structures. In Table 2, we list the optimized shortest bond lengths b_i between Fe and neighboring atoms in the flat and bent (8,0), (5,5), and (7,0) cluster models. The calculations show that, in the presence of Fe in the 2N-substituted structures, the nitrogen atoms are displaced out of the carbon surface by 0.23−0.57 Å. The elevation of the Fe atom above the CNT surface varies in the range of 1.12−2.0 Å. If the two nitrogens are farther apart, the Fe coordinates only to one of them, as in the configuration (1-3) in the (5,5) and (8,0) CNTs. However, in these cases, Fe is also bound to one or more C atoms of the nanotube, resulting in larger distances between the second N and Fe. In these structures, the Fe coordination can vary from two N to one N and two C atoms. Further increase of the N−N separation leads to a poor Fe−N coordination and related inability to form N−Fe−N bridging. This effect is manifested in the (1-4), (2-5), and (3-5) structures, as shown in Table 2. In most cases, the Fe and N atoms are displaced outward, as a result of the Fe−N bond relaxation. These displacements depend on the Fe-coordination, positions

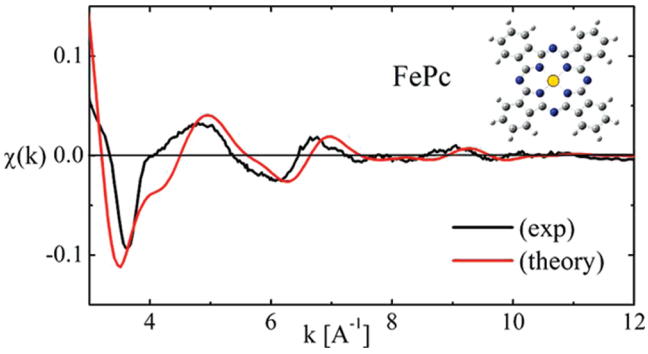

Figure 4. Comparison of the reference compounds. The black line is the experimental curve, and the red line represents the calculated spectrum of iron phthalocyanine (FePc).

of N atoms, and the cluster curvature. However, very high curvature could eventually allow to incorporate an Fe atom into the cluster, as seen in the (1-3) configuration of the (7,0) CNT (see Table 2).

The first and second atomic shells in Fe-4N configurations are the same as those in porphyrins, which have four equivalent Fe−N bonds and D_{4h} symmetry. The embedded Fe-4N sites also have four nearly equivalent bonds, but the 4N site has a rectangular shape because of the honeycomb lattice and further distortions due to nanotube curvature. The calculated bond lengths are close to those of porphyrins, which are 1.98−2.00 Å.[49] For example, the N atoms of the AX PD (8,0) site form a rectangle with an Fe atom in its center. The central atom is displaced out of the plane by 0.41 Å, whereas in the case of AX PL of the same curvature, it is shifted just by 0.15 Å. Similar displacement trends are observed in the other studied clusters. The out-of-plane displacement of Fe is larger in pyridinic than in pyrrolic configurations. In addition, axial PL sites, shown in Figure 1e, have, in general, shorter bonds than those of PD sites. This is also evident from the significantly increased Fe adsorption energies, as shown in the Table 1 (down). The axial configurations of PL sites display the same energy dependence on curvature as the PD sites. However, in the case of PL sites, the HE configurations have more extended Fe−N bond lengths and possess smaller adsorption energies.

Experimental Verification

Recently, simultaneous doping of CNTs by Fe and N was experimentally realized.[21] The structure of the active sites was characterized using X-ray absorption near-edge spectroscopy (XANES) and extended X-ray absorption fine structure (EXAFS) at the energy of the Fe K-edge. We compare the χ-functions extracted from the EXAFS data with the calculated data from our optimized structures. An ab initio multiple scattering model of EXAFS implemented in the FEFF 7.0 package is used.[50]

In Figure 4, we compare the experimental and calculated EXAFS spectrum of Fe(II) phthalocyanine used as a reference compound, where the theoretical spectrum is based on our optimized structure. The calculated spectrum is shifted by 0.46 $Å^{-1}$ to equally match the first and the second minima in the experimental spectrum. In our calculations, a scattering path of 5.5 Å is used, which includes atoms up to the second-nearest-neighbor of iron. We also include thermal motion and attenuate amplitude of $\chi(k)$ by using the Debye−Waller factors determined for phthalocyanine,[51] $\sigma^2 = 0.005$ $Å^2$. FEFF calculations with the same parameters and same shift are performed for all the structures from the previous sections.

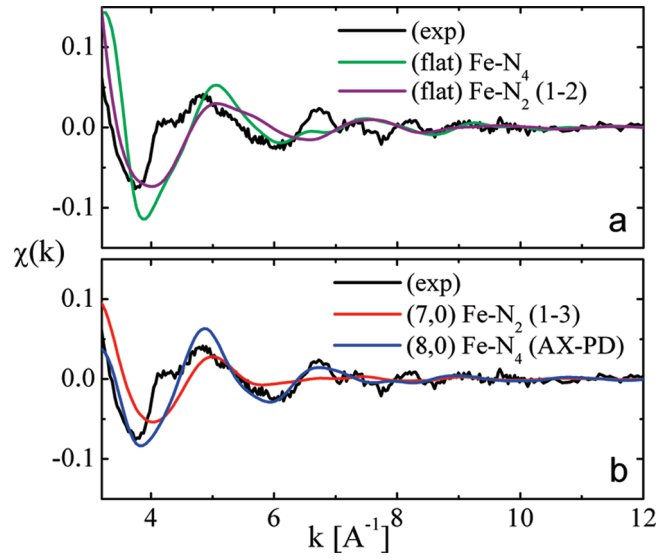

Figure 5. (a) Absorption coefficient functions $\chi(k)$ are calculated for the theoretical optimized structures. The results for flat graphene structures are compared with the $\chi_{exp}(k)$. (b) The χ functions of the bent structures with the lowest energy are compared with the experimental results.

In Figure 5a,b, we show the absorption coefficient functions $\chi(k)$ extracted from the EXAFS spectra of the experimentally prepared catalytic Fe-*x*N sites in aligned CNTs. These experimental results are compared with our simulations using the FEFF package for the optimized Fe-2N and Fe-4N structures. The Fe-*x*N structures with the lowest substitution energy, namely, (8,0) Fe-4N (AX PD) and (7,0) Fe-2N (1-3) structures shown in Figure 3 and Table 1, provide a close match with the peaks of the experimental χ functions. The amplitude and the width of the first two peaks of the Fe-4N structure correspond better to the experimental data. The similarity of the simulated spectra for the Fe-4N and Fe-2N does not exclude the possibility that the experimentally prepared structures can have both the Fe-2N and the Fe-4N structures, although the latter are more stable. From spectroscopic studies in the work of Dodelet and co-workers[14,52] it was concluded that both Fe-2N and Fe-4N might coexist in the carbon-supported materials with a ratio determined by preparation conditions, in agreement with our findings.

Summary

We reported ab initio studies of the energetics and the geometries of the metal-nitrogen sites in CNTs and compared the simulated EXAFS spectra based on the ab initio geometries to our experimental results. The studies show that the iron atom binding energy in both Fe-2N and Fe-4N configurations is much higher than that on pristine carbon nanotubes, suggesting that N stabilizes Fe on CNTs. In the case of Fe-2N configurations, the binding energy is generally lower than that in Fe-4N configurations. In the case of Fe-4N configurations, theoretical results show that the pyridinic configurations are energetically preferred over pyrrolic configurations. The results also favor incorporation of Fe-4N sites into large-diameter nanotubes and graphene compared with small-diameter CNTs. The results provide strong evidence that the transition-metal atoms are embedded into the surface of CNTs.

The simulated EXAFS spectra using theoretical structures of Fe-N sites on the CNTs are compared with the experimental EXAFS data. Theoretical structural analysis shows inequivalence

of metal−nitrogen bonds in the Fe-4N complexes embedded into nanotubes in distinction to porphyrins, thus suggesting that a single-shell modeling of EXAFS data is an oversimplification. The most stable structures from theory provide the best agreement with the experimental spectra. We conclude that the calculated structures are the most probable catalytic sites present in the experimental systems; however, further experimental studies are needed to unambiguously prove it.

Such active sites provide unique catalytic activity not only for ORR but also for other electrocatalytic and heterogeneous catalysis applications, particularly where substrate hydrophobicity and electrical conductivity are critical. The vertical ionization potentials of Fe-N-modified nanotubes were calculated to be much smaller than those of porphyrins, implying a higher catalytic activity since O_2 binding energies are similar to those of porphyrins. This might provide insight into catalytic properties of these systems, demonstrated by a good activity for oxygen-reduction reactions.[21] The geometry of these nanoporous catalysts provides confined spaces decorated with transition-metal atoms, which offers new opportunities for shape selectivity.

Acknowledgment. The authors acknowledge the use of Argonne LCRC computer resources. Computational resources for this project have been provided in part by Molecular Science Computing Facility located at Pacific Northwest National Laboratory. A.T. acknowledges the UIC Office of Research for partial support. This work was supported by the DOE BES under Contract No. DE-AC02-06CH11357.

Supporting Information Available: Vertical ionization potential and charge on the Fe atom in the ionized sites, tables of Fe NBO charges of Fe-2N and Fe-4N structures, density of states data, geometrically optimized structures with Fe-2N and Fe-4N sites, and charges in pyrrolic and pyridinic structures. This material is available free of charge via the Internet at http://pubs.acs.org.

References and Notes

(1) Steele, B. C. H.; Heinzel, A. *Nature* **2001**, *414*, 345–352.
(2) Schultz, M. G.; Diehl, T.; Brasseur, G. P.; Zittel, W. *Science* **2003**, *302*, 624–627.
(3) Wang, B. *J. Power Sources* **2005**, *152*, 1–15.
(4) Mukerjee, S.; Srinivasan, S.; Appleby, A. J. *Electrochim. Acta* **1993**, *38*, 1661–1669.
(5) Li, H. Q.; Sun, G. Q.; Li, N.; Sun, S. G.; Su, D. S.; Xin, Q. *J. Phys. Chem. C* **2007**, *111*, 5605–5617.
(6) Fernandez, J. L.; Walsh, D. A.; Bard, A. J. *J. Am. Chem. Soc.* **2005**, *127*, 357–365.
(7) Stamenkovic, V.; Schmidt, T. J.; Ross, P. N.; Markovic, N. M. *J. Electroanal. Chem.* **2003**, *554*, 191–199.
(8) Studt, F.; Abild-Pedersen, F.; Bligaard, T.; Sorensen, R. Z.; Christensen, C. H.; Norskov, J. K. *Science* **2008**, *320*, 1320–1322.
(9) Sanders, J. K. M.; Bampos, N.; Clyde-Watson, Z.; Darling, S. L.; Hawley, J. C.; Kim, H.-J.; Mak, C. C.; Webb, S. J. *The Porphyrin Handbook*; Academic Press Inc.: San Diego, CA, 1999.
(10) Lever, A. B. P.; Wilshire, J. P. *Can. J. Chem.* **1976**, *54*, 2514–2516.
(11) Jasinski, R. *Nature* **1964**, *201*, 1212.
(12) Yeager, E. *Electrochim. Acta* **1984**, *29*, 1527–1537.
(13) Easton, E. B.; Bonakdarpour, A.; Dahn, J. R. *Electrochem. Solid-State Lett.* **2006**, *9*, A463–A467.
(14) Lefevre, M.; Dodelet, J. P. *Electrochim. Acta* **2003**, *48*, 2749–2760.
(15) Maruyama, J.; Abe, I. *J. Electrochem. Soc.* **2007**, *154*, B297–B304.
(16) Jaouen, F.; Charreteur, F.; Dodelet, J. P. *J. Electrochem. Soc.* **2006**, *153*, A689–A698.
(17) Medard, C.; Lefevre, M.; Dodelet, J.; Jaouen, F.; Lindbergh, G. *Electrochim. Acta* **2006**, *51*, 3202–3213.
(18) Wang, H.; Cote, R.; Faubert, G.; Guay, D.; Dodelet, J. P. *J. Phys. Chem. B* **1999**, *103*, 2042–2049.
(19) Natarajan, S. K.; Cossement, D.; Hamelin, J. *J. Electrochem. Soc.* **2007**, *154*, B310–B315.
(20) Maldonado, S.; Stevenson, K. J. *J. Phys. Chem. B* **2005**, *109*, 4707–4716.
(21) Yang, J.; Liu, D.-J.; Kariuki, N. N.; Chen, L. X. *Chem. Commun.* **2008**, 329–331.
(22) Feng, Y. J.; He, T.; Alonso-Vante, N. *Chem. Mater.* **2008**, *20*, 26–28.
(23) Susac, D.; Zhu, L.; Teo, M.; Sode, A.; Wong, K. C.; Wong, P. C.; Parsons, R. R.; Bizzotto, D.; Mitchell, K. A. R.; Campbell, S. A. *J. Phys. Chem. C* **2007**, *111*, 18715–18723.
(24) Lee, K.; Zhang, L.; Zhang, J. J. *Electrochem. Commun.* **2007**, *9*, 1704–1708.
(25) Vayner, E.; Sidik, R. A.; Anderson, A. B.; Popov, B. N. *J. Phys. Chem. C* **2007**, *111*, 10508–10513.
(26) Ishihara, A.; Lee, K.; Doi, S.; Mitsushima, S.; Kamiya, N.; Hara, M.; Domen, K.; Fukuda, K.; Ota, K. *Electrochem. Solid-State Lett.* **2005**, *8*, A201–A203.
(27) Doi, S.; Ishihara, A.; Mitsushima, S.; Kamiya, N.; Ota, K. I. *J. Electrochem. Soc.* **2007**, *154*, B362–B369.
(28) Liu, Y.; Ishihara, A.; Mitsushima, S.; Kamiya, N.; Ota, K. *J. Electrochem. Soc.* **2007**, *154*, B664–B669.
(29) Kim, J. H.; Ishihara, A.; Mitsushima, S.; Kamiya, N.; Ota, K. I. *Electrochim. Acta* **2007**, *52*, 2492–2497.
(30) Bashyam, R.; Zelenay, P. *Nature* **2006**, *443*, 63–66.
(31) Borup, R.; et al. *Chem. Rev.* **2007**, *107*, 3904–3951.
(32) Charreteur, F.; Jaouen, F.; Ruggeri, S.; Dodelet, J.-P. *Electrochim. Acta* **2008**, *53*, 2925–2938.
(33) Matter, P. H.; Wang, E.; Arias, M.; Biddinger, E. J.; Ozkan, U. S. *J. Mol. Catal. A* **2007**, *264*, 73–81.
(34) Yang, J.; Liu, D.-J. *Carbon* **2007**, *45*, 2845–2848.
(35) Liu, D.-J.; Yang, J.; Gosztola, D. J. *ECS Trans.* **2007**, *5*, 147–154.
(36) Jain, M.; Chou, S.; Siedle, A. *J. Phys. Chem. B* **2006**, *110*, 4179–4185.
(37) Sidik, R. A.; Anderson, A. B.; Subramanian, N. P.; Kumaraguru, S. P.; Popov, B. N. *J. Phys. Chem. B* **2006**, *110*, 1787–1793.
(38) Stoyanov, S. R.; Král, P.; Wang, B. Y. *Appl. Phys. Lett.* **2007**, *90*, 153110.
(39) Stoyanov, S. R.; Král, P. *J. Phys. Chem. B* **2006**, *110*, 21480–21486.
(40) Stoyanov, S. R.; Král, P. *J. Chem. Phys.* **2008**, *129*, 234702–234710.
(41) Sternberg, M.; Curtiss, L. A.; Gruen, D. M.; Kedziora, G.; Horner, D. A.; Redfern, P. C.; Zapol, P. *Phys. Rev. Lett.* **2006**, *96*, 075506.
(42) Frisch, M. J.; et al. *Gaussian 03*, revision C.02; Gaussian, Inc.: Wallingford, CT, 2004.
(43) Kang, H. S.; Jeong, S. *Phys. Rev. B* **2004**, *70*, 233411.
(44) Zagal, J.; Bindra, P.; Yeager, E. *J. Electrochem. Soc.* **1980**, *127*, 1506–1517.
(45) Kresse, G.; Hafner, J. *Phys. Rev. B* **1993**, *47*, 558–561.
(46) Kresse, G.; Furthmuller, J. *Phys. Rev. B* **1996**, *54*, 11169–11186.
(47) Berkowitz, J. *J. Chem. Phys.* **1979**, *70*, 2819–2828.
(48) Gao, R.; Pan, Z.; Wang, Z. L. *Appl. Phys. Lett.* **2001**, *78*, 1757–1759.
(49) Shi, Z.; Zhang, J. J. *J. Phys. Chem. C* **2007**, *111*, 7084–7090.
(50) Rehr, J. J.; Deleon, J. M.; Zabinsky, S. I.; Albers, R. C. *J. Am. Chem. Soc.* **1991**, *113*, 5135–5140.
(51) Kim, S.; Ohta, T.; Kwag, G. *Bull. Korean Chem. Soc.* **2000**, *21*, 588–594.
(52) Lefevre, M.; Dodelet, J. P.; Bertrand, P. *J. Phys. Chem. B* **2002**, *106*, 8705–8713.

JP810792D